

Microchannel and Nanofiber Array Morphology Enhanced Rapid Superspreading on Animals' Corneas

Weining Miao, Shuang Zheng, Jiajia Zhou, Bo Zhang, Ruochen Fang, Dezhao Hao, Li Sun, Dianyu Wang, Zhongpeng Zhu, Xu Jin, Ye Tian,* and Lei Jiang

The dynamic spreading phenomenon of liquids is vital for both understanding wetting mechanisms and visual reaction time-related applications. However, how to control and accelerate the spreading process is still an enormous challenge. Here, a unique microchannel and nanofiber array morphology enhanced rapid superspreading (RSS) effect on animals' corneas with a superspreading time (ST) of 830 ms is found, and the respective roles of the nanofiber array and the microchannel in the RSS effect are explicitly demonstrated. Specifically, the superspreading is induced by in-/out-of-plane nanocapillary forces among the nanofiber array; the microchannel is responsible for tremendously speeding up the superspreading process. Inspired by the RSS strategy, not only is an RSS surface fabricated with an ST of only 450 ms, which is, respectively, more than 26 and 1.8 times faster than conventional superamphiphilic surfaces and animal's corneas and can be applied as RSS surfaces on video monitors to record clear videos, but also it is demonstrated that the RSS effect has tremendous potential as advanced ophthalmic material surfaces to enhance its biocompatibility for clear vision.

Learning from nature has been considered to be the most effective way to design and fabricate advanced surfaces with fantastic


Dr. W. Miao, Dr. S. Zheng, Dr. D. Hao, Prof. Y. Tian, Prof. L. Jiang
 Key Laboratory of Bioinspired Smart Interfacial Science
 Technical Institute of Physics and Chemistry
 Chinese Academy of Sciences
 Beijing 100190, China
 E-mail: tianyely@iccas.ac.cn

Dr. W. Miao, Dr. D. Hao, Prof. Y. Tian, Prof. L. Jiang
 School of Future Technology
 University of Chinese Academy of Sciences
 Beijing 100049, China

Prof. J. Zhou, Dr. R. Fang, L. Sun, Dr. D. Wang, Dr. Z. Zhu, Prof. L. Jiang
 School of Chemistry
 Beihang University
 Beijing 100191, China

Dr. B. Zhang
 Beijing Key Laboratory of Lightweight Multi-Functional Composite
 Materials and Structures
 Institute of Advanced Structure Technology
 Beijing Institute of Technology
 Beijing 100081, China

Prof. X. Jin
 Research Institute of Petroleum Exploration and Development
 PetroChina
 Beijing 100191, China

 The ORCID identification number(s) for the author(s) of this article can be found under <https://doi.org/10.1002/adma.202007152>.

DOI: 10.1002/adma.202007152

and distinguished superwettability.^[1–6] In the past, various superwetable surfaces have been found and artificially reproduced.^[7–10] However, much attention is paid to the dynamic behaviors of liquids on superhydrophobic surfaces,^[11–13] while, the liquid dynamic spreading processes on superhydrophilic surfaces are rarely investigated, a more vital phenomenon for human visual reaction time-related practical applications^[14] such as the lens of medical endoscopes, reversing cameras on driverless automobiles, biomimetic eyes, etc., whose superspreading time (ST, the time required for a water droplet to be completely spread out until the contact angle (CA) approaches 0° and a 2 μ L droplet is preferred in the paper) should be less than 1 s in order to avoid the persistence of vision,^[15] obtain clear visions, and insure security. And even though in the few researches about dynamic spreading, the STs on these

reported surfaces are very long (>5 s),^[16,17] which greatly restricts their practical applications for clear visions because the long ST is fatal in these cases of high-risk and high-speed motions. As a result, it is very urgent to understand the mechanism of liquid dynamic spreading^[18,19] and propose methods to artificially control and accelerate the spreading speeds.

Herein, we studied the corneas of New Zealand white rabbits and found that they possess not only static superamphiphilicity but also an unique rapid superspreading (RSS) effect, which refers to that a 2 μ L water droplet can be completely spread out until the CA approaches 0° within ST of 830 ms to generate a less than \approx 200 nm thick film (half of the shortest wavelength of visible light) over the nanofiber array. And it should be noted that we have further demonstrated and clearly specified the respective roles of the nanoscale and microscale structures in the RSS effect from both artificial experimental and theoretical perspectives. In detail, the superspreading is endowed by the nanofiber array and the spreading speed is dominated by the microchannel. The new effect is further applied not only as bioinspired poly(vinyl alcohol) (PVA) hydrogels with ST of only 450 ms, which outperforms respectively more than 26 and 1.8 times than conventional superamphiphilic surface^[16] and animal's cornea and show practical applications as RSS surfaces for video monitors that usually experience dramatic changes in humidity and temperature and suddenly generate large amounts of droplets need to be spread out in a very short time to record clear videos and insure security, but also as

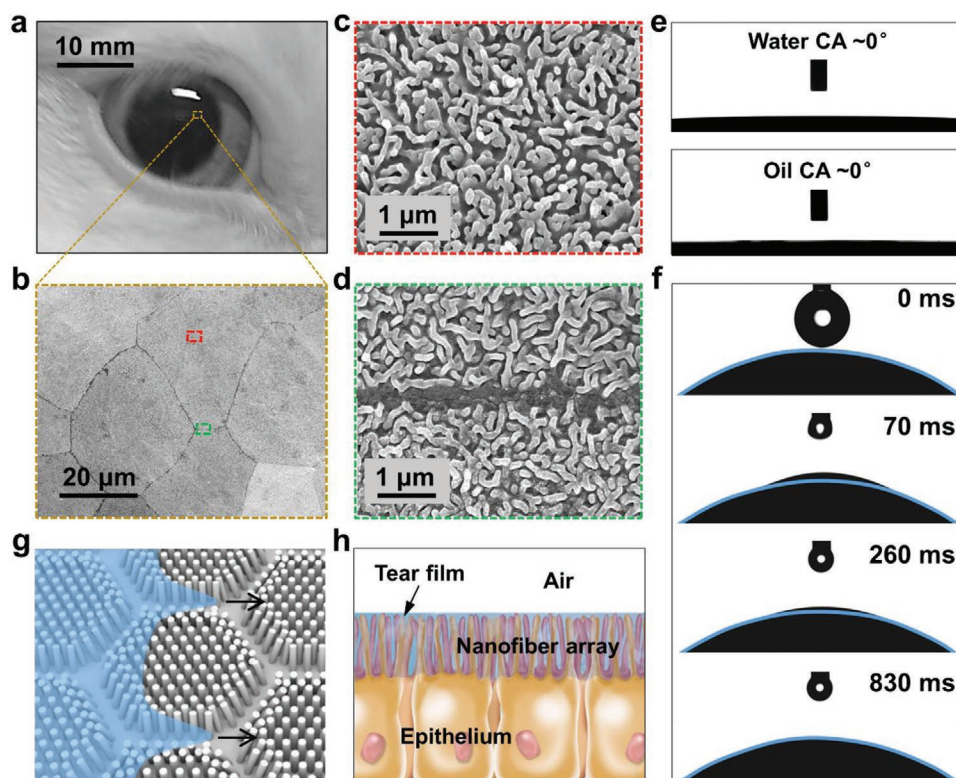


Figure 1. Morphology and RSS phenomenon on cornea. a–d) Optical photo and scanning electron microscopy (SEM) images of the rabbit cornea. SEM images suggest that the rabbit cornea surface is endowed with well-distributed nanofiber array with diameter of 88.5 ± 3.6 nm and length of 300–800 nm and the hexagonal microchannels with side length of 5.5–18.0 μm and width of 0.47 ± 0.13 μm . e) CAs of water (PBS) and oil (triglyceride) on the cornea surface are all close to 0° , indicating the cornea is superamphiphilic in air. f) A 2 μL water droplet can completely spread out to CA of 0° on cornea within 830 ms, showing the unique RSS character of the cornea. g) Schematic of the microchannel and nanofiber array morphology and the special cooperative liquid superspreading process on the cornea. h) Schematic of a uniform and thin tear film on the cornea surface, mainly containing water and oily liquid, such as phospholipids, triglyceride, etc., providing a smooth and powerful refracting surface for clear visions with rapid response time.

biomimetic superspreading silicone hydrogels (BSHs) that can exhibit obvious improvements in wettability, comfort, and biocompatibility and own tremendous potentials as advanced ophthalmic material surfaces.

The unique RSS property (Movie S1, Supporting Information) of rabbit corneas for clear visions is endowed by the special microchannel and nanofiber array morphology (Figure 1a,b; Figure S1, Supporting Information), among which the outmost parts are the polygonal microdomain, which is composed of ≈ 90 nm diameter and 300–800 nm length hydrophobic epithelium nanofiber array^[20] (Figure 1c) whose top is anchored with hydrophilic mucins,^[21] and the microchannel with length ranging from 5.5 to 18.0 μm and width of 0.47 ± 0.13 μm (Figure 1d). Resulting from such morphology and amphiphilic compositions, the CAs of both water (phosphate buffer saline solutions, PBS) and oil (tricaprylin,^[22] a kind of triglyceride produced by the meibomian glands in eye^[23]) on cornea were all close to 0° (Figure 1e). Most importantly, the ST on the cornea was only 830 ms (Figure 1f), concretely revealing the RSS property. To elucidate the process and mechanism of dynamic liquid superspreading on the cornea, we derived a simplified morphology model, i.e., on the cornea surface, there exists periodical polygonal nanofiber array microdomains that are separated by microchannels, which were artificially duplicated

to investigate their respective roles in the RSS effect as follows (Figure 1g,h).

Soft BSH nanofiber arrays similar to that on the cornea were first fabricated to investigate the role of the nanofiber array in the RSS effect. For mimicking the ingenious composition of cornea surface, i.e., hydrophilic mucins^[24] are anchored onto hydrophobic epithelium nanofiber array,^[20] oleophilic silicone monomer 3-(methacryloyloxypropyl)tris(trimethylsiloxy)silane (SiM), and hydrophilic monomers *N*-vinylpyrrolidone (NVP) (Figure 2a) were selected as components to fabricate BSH. In order to obtain the analogous nanofiber array morphology (Figure 2d,e), porous anodic aluminum oxide (AAO) templates^[25] with pore diameter of 92.1 ± 7.4 nm and center-to-center spacing of 140.0 ± 11.5 nm were utilized (Figure S2, Supporting Information). After measuring CAs of water and oil on BSH nanofiber array with varying lengths and SiM contents (Figures S3 and S4, Supporting Information), we found that there existed threshold conditions for superspreading on BSH nanofiber array, i.e., when the nanofiber length was larger than ≈ 2.12 μm and SiM content was less than 40%, the water and oil could superspread to CAs of $\approx 0^\circ$ (Figure 2b,c), resulting that the fabricated BSH was highly transparent (Figure 2f). In detail, when ω was less than 40%, BSH with ≈ 2.12 μm length nanofiber was superamphiphilic and more

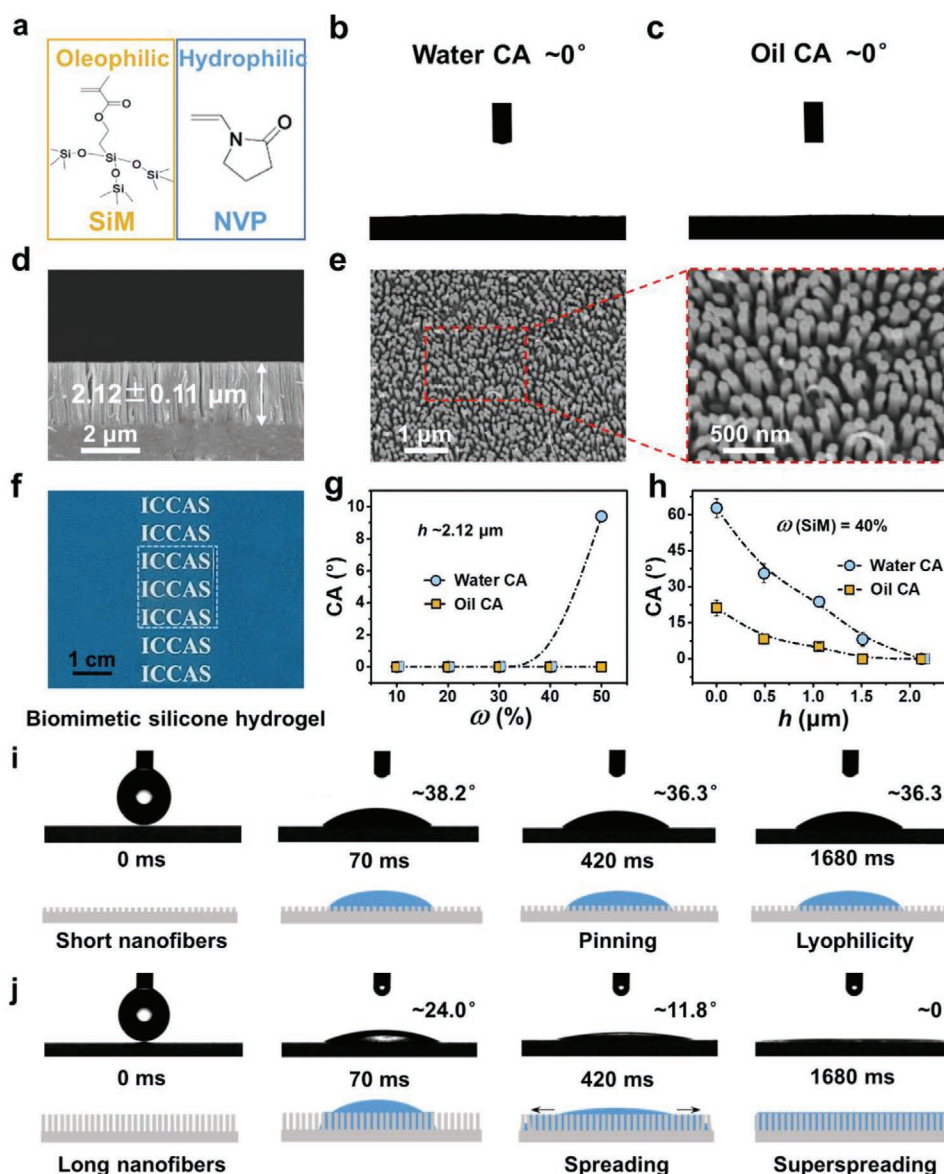


Figure 2. Threshold length for superspreading on biomimetic silicone hydrogel (BSH) nanofiber array. a) Mimicking the compositions of cornea surface, oleophilic SiM, and hydrophilic NVP are selected as components to fabricate BSH nanofiber array. b,c) CAs of water and oil illustrate that the BSH with $\approx 2.12 \mu\text{m}$ length nanofiber array is superamphiphilic. d,e) Side-view and top-view SEM images of the nanofiber array, with an averaged diameter of $\approx 90 \text{ nm}$. f) Optical image of a fabricated BSH. g) CAs of water and oil on BSH with $\approx 2.12 \mu\text{m}$ length nanofiber array as a function of SiM mass fraction (ω). CA of water increases with ω and 40% is the maximum acceptable mass fraction to ensure that superspreading can occur and the BSH is superamphiphilic. h) Variation in CA of water and oil on 40%-SiM BSHs as a function of nanofiber length (h). Longer nanofiber results in better hydrophilicity and oleophilicity and $\approx 2.12 \mu\text{m}$ length nanofiber array is able to reduce the water and oil CAs to nearly 0° . i,j) CA snapshots and schematics showing the dynamic spreading processes on BSH with shorter nanofiber array (length, $\approx 0.5 \mu\text{m}$) and longer nanofiber array (length, $\approx 2.12 \mu\text{m}$), respectively. On longer nanofiber arrays, liquids can completely spread out until the CA approaches nearly 0° , while the water CA on shorter nanofiber array is $\approx 36.3^\circ$. The error bars represent the standard deviations ($n = 3$).

SiM would obviously increase the water CA due to the hydrophobicity of SiM monomer (Figure 2g), which is readily comprehensible.

It should be noted that the length had an obvious effect on the dynamic superspreading property of nanofiber array (Figure 2h), and the threshold length for ensuring superspreading is $\approx 2.12 \mu\text{m}$. On shorter nanofiber array (length, $\approx 0.5 \mu\text{m}$), pinning happened soon with a contact angle of $\approx 36.3^\circ$

(Figure 2i; Movie S2, Supporting Information). Various, a same volume water droplet was able to superspread within $\approx 1680 \text{ ms}$ with a contact angle of $\approx 0^\circ$ on longer ones (length, $\approx 2.12 \mu\text{m}$; Figure 2j; Movie S3, Supporting Information). In contrast, the water and oil CAs on flat BSH with the same SiM content were $\approx 62.8^\circ$ and $\approx 21.2^\circ$, respectively (Figure S5, Supporting Information). The existence of the threshold length indicated that the out plane nanocapillary force played a key

role in the superspreading and the synergy of in-/out-of-plane nanocapillary forces among nanofiber array resulted in the superspreading. The lattice Boltzmann method (detailed in the Supporting Information) was carried out to further investigate the liquid spreading process on nanofiber with different lengths, and it was indicated that on shorter nanofibers ($H = 1$ and 2), pinning of the three-phase contact line stopped liquid superspreading (Figure S6a, Supporting Information); while on longer ones ($H = 3$ and 4), liquids could smoothly wet the surface and advance forward (Figure S6d, Supporting Information), which was consistent with the experimental results. And dynamic spreading processes (Figure S7, Supporting Information) on BSH with different length nanofiber array were also quantitatively investigated to verify the role of nanofiber length in superspreading.^[26] It was exhibited that the spreading area was enhanced by increasing the length of nanofiber: a water droplet (2 μ L) can spread for ≈ 23.72 mm² on BSH (nanofiber length, ≈ 2.12 μ m), compared with that of ≈ 11.02 mm² on flat silicone hydrogels. In brief, only on nanofiber array with lengths longer than a threshold value can the synergy of in-/out-of-plane nanocapillary forces be maximized to endow the surface with superspreading character.

In order to understand the role of microchannel in the RSS effect from experimental perspective, lateral dynamic spreading processes and in situ microscopy observations on hydrogels with flat, microchannel, nanofiber array, and microchannel and nanofiber array surfaces were compared. For improving the difference in the comparison results and controlling the variables more easily, the more hydrophilic and single-component artificial PVA hydrogel^[27] was chosen as the substrate material. The nanofiber array was obtained through the above-mentioned method and the microchannels (scanning electron microscopy (SEM) images in Figure 3b,d) were imprinted by triangular prismatic poly(bisphenol A polycarbonate) plates that were demolded from potassium hydroxide etched silicon wafers (Figure S8, Supporting Information). And the morphology differences between the BSH nanofiber array and PVA hydrogel nanofiber array was resulted from their distinguished mechanical properties (Figure S9, Supporting Information). As controls, we first tested and observed the dynamic spreading processes on flat and microchannel-shaped PVA hydrogels. It was shown that the CA of water on flat PVA hydrogel was $\approx 24.3^\circ$ (Figure 3a; Movie S4, Supporting Information), and on microchannel-shaped PVA, the CA could be reduced to $\approx 21.1^\circ$ (Movie S6, Supporting Information) although the water spreading speed along microchannel was faster than that on flat region (Figure 3b; Movies S5 and S7, Supporting Information). And then the lateral dynamic spreading processes on nanofiber array and microchannel and nanofiber array were studied. We found that a 2 μ L water droplet could superspread to CA of 0° within 2.15 s on nanofiber array (Figure 3c; Movie S8, Supporting Information). Unexpectedly, the ST on microchannel and nanofiber array could be accelerated to only 450 ms (Figure 3d; Movie S10, Supporting Information), achieving an RSS surface that is more than 26 and 1.8 times faster than conventional superamphiphilic surface^[16] and animal's cornea, respectively. In situ microscopy movies revealed that the acceleration in ST was ascribed to the fact that the superspreading speed along the microchannel was higher than that

in nanofiber array domain and the meniscus formed between neighboring microchannels further guided and accelerated the advancing process of three-phase contact line (Movies S9 and S11, Supporting Information). These comparative results demonstrated that the superspreading of the cornea was endowed by the nanofiber array region and the RSS character of the cornea was dominated by the microchannels from artificial experimental perspective (Figure 3e). Besides, we studied the effect of angle between microchannels (α), pitch of neighboring microchannels (d), and the curvatures (K) of the surfaces, on the dynamic superspreading property and concluded that the ST would increase with d significantly (Figure 3f), while α and K had little effects on the ST (Figure S10–S12 and Movies S12, Supporting Information), which could further guide the practical design of practical RSS surfaces.

In order to further clarify the underlying mechanism from theoretical perspective, simplified nanofiber array and microchannel and nanofiber array morphology models were built and mathematical analysis of superspreading process was carried out (Figure 3g). We compared the spreading speeds on microchannel and nanofiber array (V_{ii}) and nanofiber array (V_i) by Equation (1) derived from Equations (S12) and (S16) in the Supporting Information

$$\frac{V_{ii}}{V_i} = \frac{L_{ii}}{L_i} = \sqrt{\frac{w \left(\cos \theta_E - \sin \frac{\beta}{2} \right) f(c)}{r \cos \theta_E \lambda(\beta)}} \quad (1)$$

Here, $\theta_E < \pi - \beta/2$ is the sufficient condition for the liquid to wet the microchannel, where θ_E is the intrinsic contact angle of substrate. For hydrophilic surfaces, i.e., $\theta_E < \approx 65^\circ$,^[28] the speed ratio is larger than 1 and the RSS effect will become more distinctive with the improvement in substrate hydrophilicity (Figure 3h). The calculation results further confirmed the respective roles of the microchannel and the nanofiber array in the RSS effect and guide the selection of more hydrophilic PVA hydrogel above-mentioned. From the other point of view, the spreading speed on microchannel and nanofiber array is relatively larger even when the roughness is smaller (Figure 3c,d,g), compared with those of nanofiber array, which is contrary to the prediction according to roughness, illustrating that the rapid superspreading process is a synergetic result of thermodynamics and kinetics. Besides, the ratio of liquid flow rates in microchannel and nanofiber array (Q_{ii}) and nanofiber array (Q_i) can be deduced

$$\frac{Q_{ii}}{Q_i} = \frac{S_{ii} V_{ii}}{S_i V_i} \quad (2)$$

where S_{ii} and S_i are the cross-sectional areas of microchannel and nanofiber array and nanofiber array, respectively. Since the S_{ii} is larger than S_i (see the Supporting Information), the liquid flow rate is increased more obviously than the spreading speed. As a result, the large liquid flow rate and fast superspreading speed can be achieved on the new morphology at the same time.

And such microchannel and nanofiber array strategy that combines large liquid flow rate and rapid spreading speed

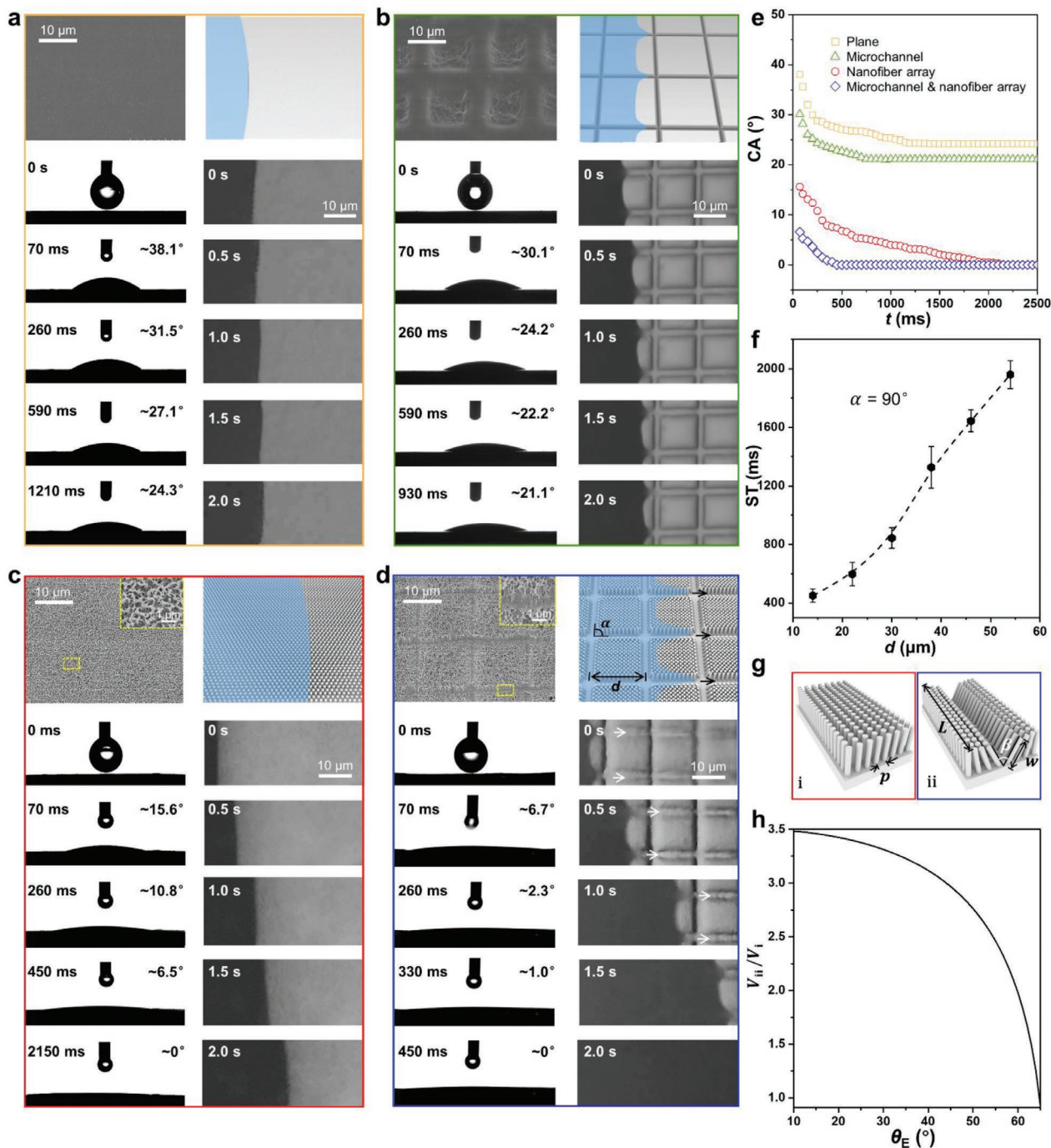


Figure 3. Respective roles of microchannel and nanofiber array in RSS effect. a,b) Lateral views and in situ microscopy movies of dynamic spreading process of a 2 μL water droplet on flat and microchannel-shaped PVA hydrogels, respectively. A droplet can spread to steady state within 1.21 and 0.93 s on plane and microchannel with contact angle of $\sim 24.3^\circ$ and 21.1° , respectively. Water spreading speed along microchannel is faster than that on flat region. c) Dynamic superspreading process of a same volume water droplet on ~ 90 nm diameter and ~ 500 nm length PVA nanofiber array. The ST is 2.15 s. d) A water droplet of the same volume can superspread to CA of 0° within only 450 ms on the microchannel and nanofiber array surface. In situ microscopy imaging demonstrates that the RSS character is attributed to the fact that the higher spreading speed along the microchannels accelerates the spreading process on nanofiber array domains. SEM images of the microchannel and nanofiber array morphology and the corresponding simplified schematic are exhibited. α and d are angle and pitch of microchannels, respectively. e) Variation in CA on plane, microchannel, nanofiber array, and microchannel and nanofiber array as a function of time. Only when microchannel and nanofiber array coexist, can RSS occur, showing potentials as RSS surfaces for video monitors; in the absence of nanofiber array, microchannel alone can only slightly reduce water CA and accelerate the process of the water reaching a steady state. f) Influence of d on ST. The error bars represent the standard deviations ($n = 3$). g) Simplified models for calculations of spreading speeds and flow rates on i) nanofiber array and ii) microchannel and nanofiber array, respectively. h) The corresponding calculated ratio of speeds in (ii) and (i) as a function of intrinsic contact angle of substrate (θ_E).

could provide a brand new avenue to fabricate practical RSS surfaces (blue dots in Figure 3e) for video monitors, which usually experience dramatic changes in humidity and temperature and where the response time is a severe security concern, such as lens of medical endoscopes that will be blurred during in vivo operations; reversing cameras and rearview mirrors on current automobiles, imaging sensors on unmanned aerial vehicles, and even future driverless cars that will become obscure when driving or parking in garages. In these application scenarios, there will be generation of large amounts of liquids in a very short time that need to be spread out quickly and the rapid superspreading speed and large flux in the new morphology will work effectively; otherwise, accidents will occur. More importantly, as follows, our finding could even be utilized as biocompatible ophthalmic surfaces of contact lenses and biomimetic eyes to realize functions similar to the actual corneas.

As described before, the BSH owns component, morphology, and amphiphilicity similar to the cornea at the same time, hence, we speculated that the BSH should possess properties analogous to the natural corneas as ophthalmic materials for clear visions. Unsurprisingly, its tremendous potentials as completely wettable, comfortable, and biologically compatible surfaces for high-performance continuously wearable contact lenses and biomimetic eyes are corroborated. The latest-generation contact lenses are mainly silicone hydrogels.^[29–31] However, these contact lenses are still confronted with several disadvantages, mainly poor amphiphilicity that is important to stabilize uniform tear films on ophthalmic materials to reduce

their foreign body sensation,^[32] and poor antiprotein adhesion property that is crucial for long-term lenses.^[33] At the same time, the comfort and the biocompatibility are great challenges for biomimetic eyes to realize their practical applications. Here, we demonstrated that our RSS BSH owns excellent wettability that significantly outperforms the commercial contact lenses (Figure 4a) and long-lasting superamphiphilicity (Figure S13, Supporting Information) that could be applied as both high-performance contact lenses and more comfortable surfaces for biomimetic eyes. In addition, the BSH exhibited extremely high oxygen permeability (Figure 4b), a crucial requirement for high-performance continuously wearable contact lenses.^[32] The transparency (Figure 4c; Figure S14, Supporting Information) and water content (Figure S15, Supporting Information) of BSH, two fundamental parameters as contact lenses and biomimetic eye surfaces, were also similar to that of commercial contact lenses and biological counterparts.^[34,35] Besides, the RSS BSH showed remarkable performance in antiprotein adhesion performance (Figure 4d,e), which not only is a bottleneck of current continuously wearable contact lenses but also is vital to improve the biocompatibility of biomimetic eyes. All these results demonstrate the large potentials of the biomimetic superspreading surfaces as biocompatible ophthalmic material surfaces.

In summary, we have clearly clarified the respective roles of nanoscale and microscale structures behind the special micro-channel and nanofiber array morphology enhanced RSS effect on cornea, which contains the synergy of in-/out-of-plane

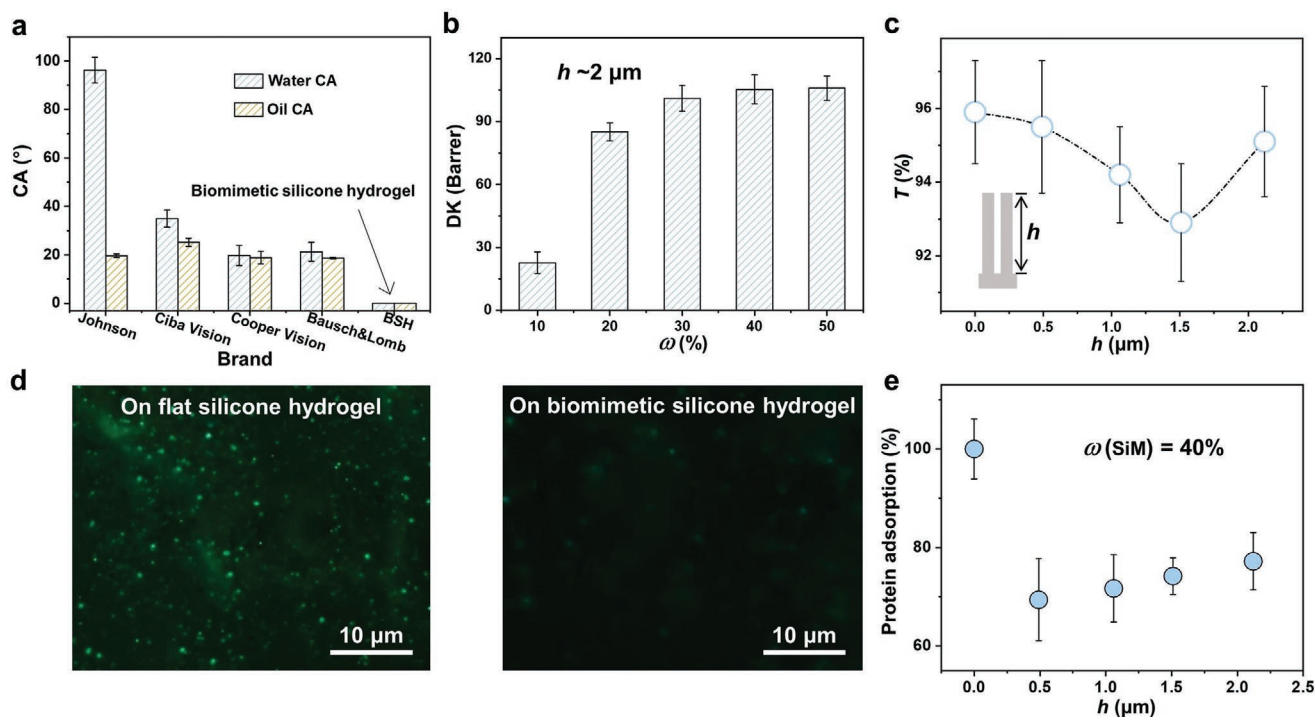


Figure 4. Biomimetic superspreading BSH as biocompatible ophthalmic materials. a) BSH exhibits better amphiphilicity than commercial contact lenses, which is crucial to maintain a stable tear film to reduce foreign body sensation and suppress inflammations as ophthalmic materials. b) Oxygen permeability coefficient (DK) of BSH as a function of SiM mass fraction. The DK reaches 105.3 Barrer when ω is equal to 40%. c) Transparency of BSH. The length of the nanofiber array has a little influence on the transmittance of hydrated BSH. d) Representative images of fluorescent-labeled protein (rhodamine-bovine serum albumin) adhered on flat silicone hydrogel and BSH, respectively. e) Ratio of adhered protein value on BSH and plane as a function of nanofiber length. Error bars represent the standard deviations ($n = 5$).

nanocapillary forces among nanofiber array that results in superspreading and the microchannel that dominates the enhancement of superspreading speed and liquid flow rate. Besides, by virtue of the deep insight in the new RSS effect, first, PVA hydrogel with ST of only 450 ms is designed, which significantly outperforms previously reported surfaces and shows impressive potentials as RSS surfaces for video monitors, such as lens of medical endoscopes, reversing cameras and rearview mirrors on current automobiles, imaging sensors on unmanned aerial vehicles, and future driverless cars; second, the BSH is further obtained, achieving large improvements in wettability, comfort, and biocompatibility, which is similar to the natural corneas when used as new ophthalmic materials surfaces for clear visions, such as high-performance continuously wearable contact lenses and biomimetic eyes. We believe that our finding and our clarification in the respective roles of nanoscale and microscale structures in the RSS effect can further guide and spark various marvelous ideas to design other wonderful high-performance surfaces.

Experimental Section

Animals: Male New Zealand white rabbits (≈ 2.5 kg) were treated according to the ARVO Statement for the Use of Animals in Ophthalmic and Vision Research and the Directive 2010/63/EU of the European Parliament and of the Council, which was approved by the Beijing Fangyuan aquaculture farm, China. Rabbits were killed via a systemic injection of sodium pentobarbital under deep anesthesia, followed by peeling off the entire cornea, which was stored in the PBS as just collected and subsequently used for the wettability tests.

Fabrication of the BSHs: SiM (98%), NVP, 2-hydroxyethyl methacrylate (HEMA), photoinitiator 2-hydroxy-2-methylbenzene acetone (D-1173), crosslinking agent poly(ethylene glycol) dimethacrylate (PEGDMA, average M_n 750), and solvent 1-hexanol were added into flask in orders (Table S1, Supporting Information), followed by vigorous stirring in dark for 30 min. Then, the mixture was added onto 1H,1H,2H,2H-perfluorodecyltriethoxysilane fluorinated AAO mold (Shanghai Shang-Mu Nano Technology, Ltd.) and cured by an LED UV curing system (UPP3-734, Utata) for 10 min at room temperature. The copolymer and the mold were purified by extraction with 1-hexanol and ethanol in turn, and then hydrated in water for 8 h. Finally, the silicone hydrogel was peeled off from the mold and stored in PBS.

Fabrication of the Bionic PVA Hydrogels: A solution mixture of PVA (Shanghai Ying-Jia Industrial Development Co., Ltd., 10 g), dimethylsulfoxide (DMSO, 67.5 g), and distilled water (22.5 g) was first prepared. Second, the solution was stirred at 90 °C until the PVA was dissolved. Third, the mixture was poured onto the AAO templates without any modifications and then was frozen for 12 h in -15 °C refrigerator. Fourth, the frozen gel was washed by distilled water for three times. Fifth, the gel was soaked in 1 wt% glutaraldehyde aqueous solution containing hydrochloric acid as catalysts for 30 min until the nanostructured nanofiber array was released from the AAO templates. And, the microchannels on hydrogel were fabricated through adjusting the angle of two successive imprinting of poly(bisphenol A polycarbonate) plates with parallel triangular prisms that were demolded from silicon wafer. Finally, the gel was washed by PBS repeatedly to get the PVA hydrogels. The water content of PVA hydrogel was 81.6%.

Characterization of the Morphology and Dynamic Spreading Process: Morphology of the cornea, PVA hydrogels, and BSH hydrogels was investigated by SEM (JEOL, JSM-7500F, Japan) at an accelerating voltage of 5.0 kV. In order to prepare samples for SEM imaging, the cornea was fixed with 4% paraformaldehyde for 24 h at room temperature and then dehydrated by a graded series of ethanol, and the hydrogel samples were frozen by liquid nitrogen and dried by a lyophilizer (CHRIST).

The lateral-view dynamic spreading processes were recorded with an i-SPEED 3 (Olympus) high-speed camera and the top-view in situ microscopy movies were recorded with an optical microscope (Vision Engineering Co.) equipped with a CCD camera connected to a computer. The surface wettability was measured with a contact-angle system (OCA 20, DataPhysics, Germany). The CAs were obtained by averaging five CAs at different positions on the same sample.

Characterization of the BSHs as Contact Lenses and Biomimetic Eyes: The oxygen permeability was determined using a permeability testing instrument (OX2, China) at a humidity of $\approx 90\%$. The light transmittance measurements were carried out with a UV-visible spectrophotometer at a wavelength range of 400–800 nm. The images of the adhered fluorescent-labeled protein (BSA, Guangdong Shun-Hao biotechnology Co., Ltd.) were obtained by a fluorescence microscope (Vision Engineering Co.). The method to measure the amount of adhered protein (BSA) on BSH was described as follows. First, a PBS solution containing 1 mg mL^{-1} BSA was prepared. Second, a BSH sample ($2\text{ cm} \times 2\text{ cm}$) was immersed into the overnight equilibrated solution at 37 °C for 2 h. Third, the sample was rinsed for five times by fresh PBS solution. Fourth, the sample was soaked into 2 mL PBS solution containing 1 wt% SDS to desorb the adhered BSA by sonication for 20 min. Finally, the BSA concentration was obtained by measuring the absorbance of quintuplicate samples and the ratio of the adhered protein value on BSH and plane was gained by dividing the concentration of BSH by that of flat silicone hydrogels.

Supporting Information

Supporting Information is available from the Wiley Online Library or from the author.

Acknowledgements

W.M. and S.Z. contributed equally to this work. This research was supported by the National Research Fund for Fundamental Key Projects (2019YFA0708702), the National Natural Science Foundation (21972154, 21988102, and 22090052), the Frontier Science Key Projects of CAS (ZDBS-LY-SLH022), and the Beijing Municipal Science & Technology Commission No. Z181100004418014 (No. Z181100004418013).

Conflict of Interest

The authors declare no conflict of interest.

Data Availability Statement

Research data are not shared.

Keywords

clear vision, cornea, microchannels, nanofiber arrays, superspreading

Received: October 20, 2020

Revised: February 23, 2021

Published online: April 23, 2021

- [1] A. R. Parker, C. R. Lawrence, *Nature* **2001**, 414, 33.
- [2] H. Chen, P. F. Zhang, L. W. Zhang, H. L. Liu, Y. Jiang, D. Y. Zhang, Z. W. Han, L. Jiang, *Nature* **2016**, 532, 85.
- [3] M. Prakash, D. Quere, J. W. M. Bush, *Science* **2008**, 320, 931.

- [4] X. Hou, Y. H. Hu, A. Grinthal, M. Khan, J. Aizenberg, *Nature* **2015**, 519, 70.
- [5] U. G. K. Wegst, H. Bai, E. Saiz, A. P. Tomsia, R. O. Ritchie, *Nat. Mater.* **2015**, 14, 23.
- [6] Q. Wang, B. Su, H. Liu, L. Jiang, *Adv. Mater.* **2014**, 26, 4889.
- [7] Y. Zheng, H. Bai, Z. B. Huang, X. L. Tian, F. Q. Nie, Y. Zhao, J. Zhai, L. Jiang, *Nature* **2010**, 463, 640.
- [8] M. Liu, S. Wang, L. Jiang, *Nat. Rev. Mater.* **2017**, 2, 17036.
- [9] X. Gao, X. Yan, X. Yao, L. Xu, K. Zhang, J. H. Zhang, B. Yang, L. Jiang, *Adv. Mater.* **2007**, 19, 2213.
- [10] Y. Xiang, S. Huang, T. Y. Huang, A. Dong, D. Cao, H. Li, Y. Xue, P. Lv, H. Duan, *Proc. Natl. Acad. Sci. USA* **2020**, 117, 2282.
- [11] Y. H. Liu, L. Moevius, X. P. Xu, T. Z. Qian, J. M. Yeomans, Z. K. Wang, *Nat. Phys.* **2014**, 10, 515.
- [12] Q. Sun, D. Wang, Y. Li, J. Zhang, S. Ye, J. Cui, L. Chen, Z. Wang, H.-J. Butt, D. Vollmer, X. Deng, *Nat. Mater.* **2019**, 18, 936.
- [13] T. Mouterde, G. Lehoucq, S. Xavier, A. Checco, C. T. Black, A. Rahman, T. Midavaine, C. Clanet, D. Quere, *Nat. Mater.* **2017**, 16, 658.
- [14] L. Gu, S. Poddar, Y. Lin, Z. Long, D. Zhang, Q. Zhang, L. Shu, X. Qiu, M. Kam, A. Javey, Z. Fan, *Nature* **2020**, 581, 278.
- [15] H. Owens, J. Phillips, *Cornea* **2001**, 20, 484.
- [16] Z. Zhu, Y. Tian, Y. Chen, Z. Gu, S. Wang, L. Jiang, *Angew. Chem., Int. Ed.* **2017**, 56, 5720.
- [17] V. Zorba, X. Chen, S. S. Mao, *Appl. Phys. Lett.* **2010**, 96, 093702.
- [18] J. Huang, Y. C. Lo, J. J. Niu, A. Kushima, X. F. Qian, L. Zhong, S. X. Mao, J. Li, *Nat. Nanotechnol.* **2013**, 8, 277.
- [19] C. Duprat, S. Protiere, A. Y. Beebe, H. A. Stone, *Nature* **2012**, 482, 510.
- [20] F. J. Holly, M. A. Lemp, *Exp. Eye Res.* **1971**, 11, 239.
- [21] P. Argueso, I. K. Gipson, *Exp. Eye Res.* **2001**, 73, 281.
- [22] A. Mastromarino, M. Papadia, V. Amico, S. Giuffrida, M. Rolando, *Invest. Ophthalmol. Visual Sci.* **2005**, 46, 2043.
- [23] A. H. Rantamaki, M. Javanainen, I. Vattulainen, J. M. Holopainen, *Invest. Ophthalmol. Visual Sci.* **2012**, 53, 6442.
- [24] A. F. Ablamowicz, J. J. Nichols, *Ocul. Surf.* **2016**, 14, 331.
- [25] W. Lee, S.-J. Park, *Chem. Rev.* **2014**, 114, 7487.
- [26] L. Courbin, E. Denieul, E. Dressaire, M. Roper, A. Ajdari, H. A. Stone, *Nat. Mater.* **2007**, 6, 661.
- [27] S. H. Hyon, W. I. Cha, Y. Ikada, *Polym. Bull.* **1989**, 22, 119.
- [28] L. Wang, Y. Zhao, Y. Tian, L. Jiang, *Angew. Chem., Int. Ed.* **2015**, 54, 14732.
- [29] M. E. Seitz, M. E. Wiseman, I. Hilker, J. Loos, M. W. Tian, J. Y. Li, M. Goswami, V. M. Litvinov, S. Curtin, M. Bulters, *Polymer* **2017**, 118, 150.
- [30] Z. Zhao, S. S. An, H. J. Xie, X. L. Han, F. H. Wang, Y. Jiang, *J. Phys. Chem. B* **2015**, 119, 9780.
- [31] G. D. Friends, J. F. Kunzler, R. M. Ozark, *Macromol. Symp.* **1995**, 98, 619.
- [32] P. C. Nicolson, J. Vogt, *Biomaterials* **2001**, 22, 3273.
- [33] C. S. A. Musgrave, F. Fang, *Materials* **2019**, 12, 261.
- [34] D. Li, S. C. G. Tseng, *J. Cell. Physiol.* **1995**, 163, 61.
- [35] R. Montes-Mico, J. L. Alio, W. N. Charman, *Invest. Ophthalmol. Visual Sci.* **2005**, 46, 1615.

ADVANCED MATERIALS

Supporting Information

for *Adv. Mater.*, DOI: 10.1002/adma.202007152

Microchannel and Nanofiber Array Morphology
Enhanced Rapid Superspreading on Animals' Corneas

*Weining Miao, Shuang Zheng, Jiajia Zhou, Bo Zhang,
Ruochen Fang, Dezhao Hao, Li Sun, Dianyuan Wang,
Zhongpeng Zhu, Xu Jin, Ye Tian,* and Lei Jiang*

Supporting Information for

**Microchannel and nanofiber array morphology enhanced rapid superspreading
on animals' corneas**

Weining Miao*, Shuang Zheng*, Jiajia Zhou, Bo Zhang, Ruochen Fang, Dezhao Hao, Li Sun,
Dianyu Wang, Zhongpeng Zhu, Xu Jin, Ye Tian†, and Lei Jiang

Supporting Text

Lattice Boltzmann method. In the LB biomimetic, both space and time are discrete, and particles move on a regular lattice by applying consecutive propagation and collision processes. In the collision process we employed the efficient BGK biomimetic, for which the speeds of all discrete distribution functions approaching equilibrium are determined by a single relaxation time τ ($\tau = 1.0$ in this work). The BGK biomimetic has advantages of keeping the most fundamental conservation laws and allowing flexibility of the transport coefficients. The general form of the lattice Boltzmann equation with the BGK approximation can be written as:

$$f_i(\mathbf{x} + \mathbf{e}_i \Delta t, t + \Delta t) = f_i(\mathbf{x}, t) - \frac{\Delta t}{\tau} [f_i(\mathbf{x}, t) - f_i^{eq}(\mathbf{x}, t)] \quad (S1)$$

with $f_i(\mathbf{x}, t)$ the density distribution function, \mathbf{e}_i the discrete velocity, and Δt the time step.

The equilibrium distribution function, $f_i^{eq}(\mathbf{x}, t)$ is given by

$$f_i^{eq}(\mathbf{x}, t) = \omega_i \rho \left[1 + \frac{\mathbf{e}_i \cdot \mathbf{u}^{eq}}{c_s^2} + \frac{(\mathbf{e}_i \cdot \mathbf{u}^{eq})^2}{2c_s^4} - \frac{\mathbf{u}^{eq^2}}{2c_s^2} \right] \quad (S2)$$

with the weight factors $\omega_i = \begin{cases} 1/3 & e_i^2 = 0 \\ 1/18 & e_i^2 = 1 \\ 1/36 & e_i^2 = 2 \end{cases}$, and the speed of sound $c_s = \sqrt{3}/3$ in lattice

unit. The density ρ is obtained with $\rho = \sum_i f_i$, the kinetic viscosity of liquid is calculated with

$\nu = c_s^2(\tau - 0.5)\Delta t$, and the macroscopic velocity is determined by $\mathbf{u}^{eq} = \mathbf{u} + \frac{\tau \mathbf{F}}{\rho}$ with

$\mathbf{u} = \frac{1}{\rho} \sum_{i=0}^{i=8} f_i \mathbf{e}_i$. \mathbf{F} contains two types of force, one is the long-range interactions for liquid-liquid,

liquid-vapor, vapor-vapor interactions are described using the same equation as follows:

$$\mathbf{F}_i(\mathbf{x}, t) = -G \psi(\mathbf{x}, t) \sum_i \omega_i \psi(\mathbf{x} + \mathbf{e}_i \Delta t, t) \mathbf{e}_i \quad (S3)$$

where G controls the strength of interacting and ψ is the interaction potential that expressed as:

$$\psi(\rho) = \psi_0 \exp\left(\frac{-\rho_0}{\rho}\right) \quad (S4)$$

with $\psi_0 = 4$ and $\rho_0 = 200$. The other is the interaction between solid and fluid:

$$F_s(x, t) = -G_s \psi(x, t) \sum_i \omega_i s(x + e_i \Delta t, t) e_i \quad (\text{S5})$$

G_s is the parameter that controls the strength of the interaction between solid and fluid sites, and $s(x + e_i \Delta t)$ is an indicator function that is equal to 1 or 0 for a solid or a fluid domain node, respectively. In our simulations bounce back boundary condition was adopted for the solid boundary.

Comparison of water dynamic spreading in nanofiber array and microchannel & nanofiber array.

We first consider dynamic spreading in the nanofiber array arranged inside the hexagonal lattice. The area fraction (c) occupied by the fibers is given by

$$c = \frac{\frac{1}{2}\pi r^2}{\frac{1}{2}p^2 \sin 60^\circ} = 0.326 \quad (\text{S6})$$

where r and p represent the radius and the pitch of nanofibers, respectively.

The evolution of the front can be derived from the Onsager principle^[1]. Assuming the wetted area has a length L and a width W , the free energy of the system is given by

$$A = -2\pi r h c W L \gamma \cos \theta_E \quad (\text{S7})$$

where γ is the surface tension of the liquid, h is the length of nanofibers and θ_E is the intrinsic contact angle of the substrate material.

The change rate of the free energy is given by

$$\dot{A} = -2\pi r h c W \dot{L} \gamma \cos \theta_E \quad (\text{S8})$$

For a hexagonal array of cylinder, the frictional force on one cylinder is given by

$$F = h f(c) \eta U \quad (\text{S9})$$

where η is the viscosity of the fluid, $U = \dot{L}$ is the dynamic spreading speed of the front, and $f(c)$ is a numerical factor^[2]. For $c = 0.326$, $f(c) \approx 100$. The dissipation Φ in the system is then

$$\Phi = \frac{1}{2} h f(c) \eta \dot{L}^2 c W L \quad (\text{S10})$$

The evolution of the dynamic spreading front is given by $\partial(\dot{A} + \Phi)/\partial \dot{L} = 0$. This leads to

$$L \dot{L} = \frac{2\pi r \gamma \cos \theta_E}{f(c) \eta} \quad (\text{S11})$$

The front propagation follows the standard Lucas-Washburn scaling

$$L_i = \sqrt{\frac{4\pi r \gamma \cos \theta_E}{f(c) \eta} t} \quad (\text{S12})$$

where L_i is the dynamic spreading distance in the nanofiber array.

Then, we examine the case where the cross section of the microchannel is a triangle. The side length of the triangle is w and its open angle is β . The fluid fills the channel with length L .

The free energy is given by

$$A = -2wL \gamma (\cos \theta_E - \sin \frac{\beta}{2}) \quad (\text{S13})$$

The change rate of the free energy is

$$\dot{A} = -2w \dot{L} \gamma (\cos \theta_E - \sin \frac{\beta}{2}) \quad (\text{S14})$$

The dissipation can be calculated using lubrication approximation

$$\Phi = \frac{1}{2}\lambda(\beta)\eta L\dot{L}^2 \quad (\text{S15})$$

where $\lambda(\beta)$ is a geometric parameter that depends only on the open angle $\beta^{[3]}$. For $\beta = 60^\circ$, $\lambda(\beta) \approx 15.97$

The evolution of the front is again given by the Onsager principle

$$L_{\text{channel}} = L_{\text{ii}} = \sqrt{\frac{4\pi w \gamma (\cos\theta_E - \sin\frac{\beta}{2})}{\lambda(\beta)\eta} t} \quad (\text{S16})$$

where L_{channel} is the dynamic spreading distance in the microchannel and is also approximately the dynamic spreading distance on microchannel & nanofiber array (L_{ii}) because that the microchannel governs the spreading speed on microchannel & nanofiber array.

Therefore, the ratio of spreading speeds on microchannel & nanofiber array (V_{ii}) and nanofiber array (V_{i}) can be concluded

$$\frac{V_{\text{ii}}}{V_{\text{i}}} = \frac{L_{\text{ii}}}{L_{\text{i}}} = \sqrt{\frac{w(\cos\theta_E - \sin\frac{\beta}{2})}{r \cos\theta_E} \frac{f(c)}{\lambda(\beta)}} \quad (\text{S17})$$

The cross-sectional area of microchannel & nanofiber array (S_{ii}) is given by

$$S_{\text{ii}} = \left(W - 2w \sin\frac{\beta}{2}\right) h \frac{(p-2r)}{2} + w^2 \sin\frac{\beta}{2} \cos\frac{\beta}{2} \quad (\text{S18})$$

The cross-sectional area of nanofiber array (S_{i}) is given by

$$S_{\text{i}} = \left(W - 2w \sin\frac{\beta}{2}\right) h \frac{(p-2r)}{2} + 2w \sin\frac{\beta}{2} h \frac{p-2r}{p} \quad (\text{S19})$$

And the ratio of liquid flow rate in microchannel & nanofiber array (Q_{ii}) and nanofiber array (Q_{i}) is given by

$$\frac{Q_{\text{ii}}}{Q_{\text{i}}} = \frac{S_{\text{ii}}V_{\text{ii}}}{S_{\text{i}}V_{\text{i}}} \quad (\text{S20})$$

Since $\cos\frac{\beta}{2} > 2\frac{p-2r}{p}$, and $w > h$. This leads to

$$S_{\text{ii}} > S_{\text{i}} \quad (\text{S21})$$

Therefore, the ratio of liquid flow rate ($\frac{Q_{\text{ii}}}{Q_{\text{i}}}$) is much larger than the ratio of spreading speeds

($\frac{V_{\text{ii}}}{V_{\text{i}}}$).

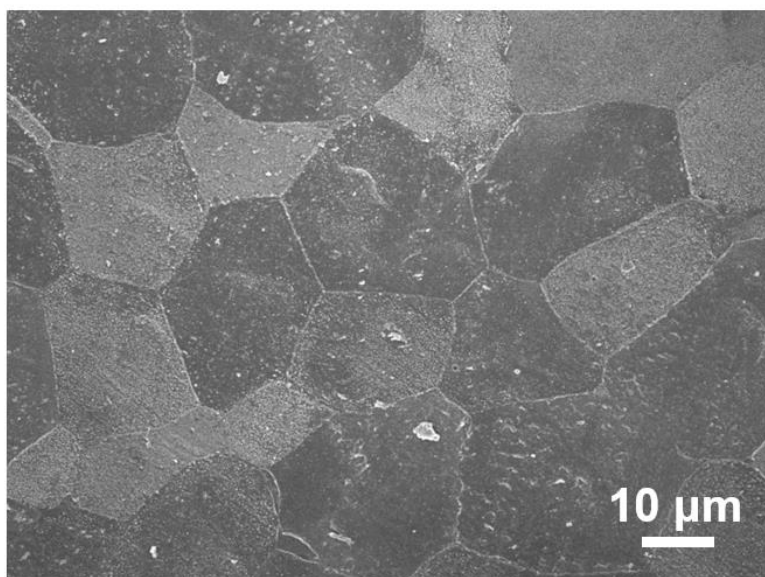


Figure S1. Large-area SEM image of the microchannel & nanofiber array morphology on the cornea surface. The nanofiber array is separated by microchannels into nearly hexagonal uniformly distributed domains.

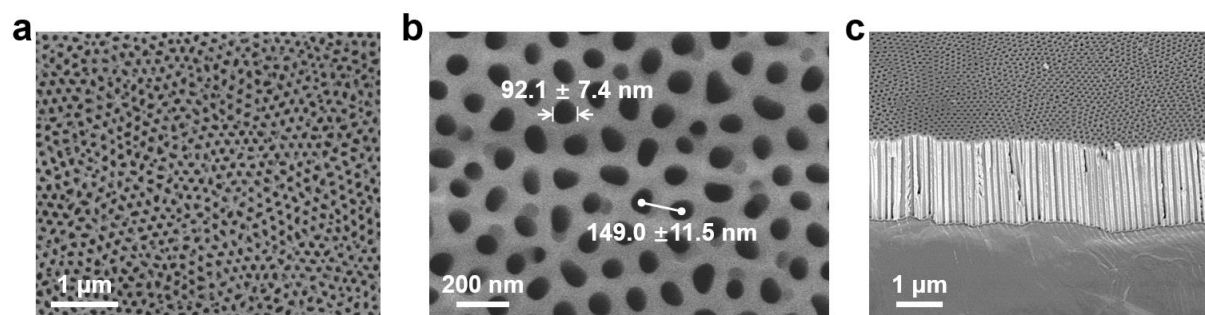


Figure S2. The template used for preparing nanofiber array. (a, b) Top-view SEM images of the AAO template with 92.1 ± 7.4 nm-diameter and 140.0 ± 11.5 nm-spacing pores. (c) Oblique-view SEM images of the AAO template.

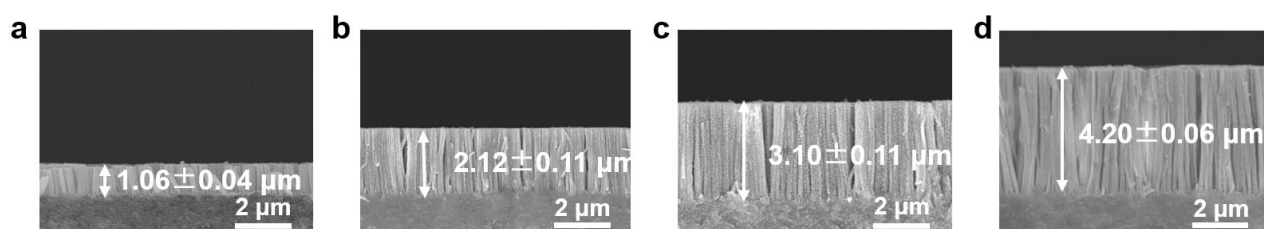


Figure S3. The fabricated BSHs with different length nanofiber array. (a-d) The lengths of BSH nanofiber are ~ 1.06 , ~ 2.12 , ~ 3.10 and ~ 4.20 μm , respectively.

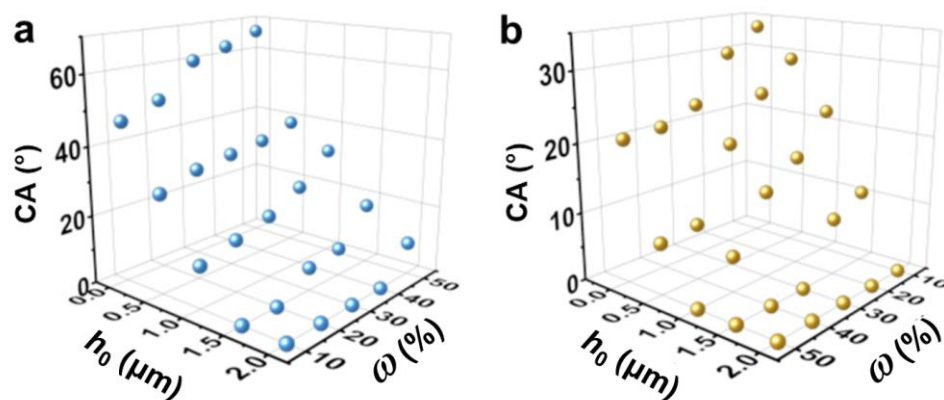


Figure S4. CAs of water and oil on the BSH. (a) Water CAs on the BSHs show that increasing the length of nanofiber or decreasing the content of SiM will enhance the hydrophilicity. (b) Oil CAs on the BSH show that increasing the length of nanofiber or increasing the content of SiM will improve the oleophilicity. Nanofiber array with the length of $\sim 2.12 \mu\text{m}$ and SiM content of 40% is suitable for fabricating superspreading BSH.

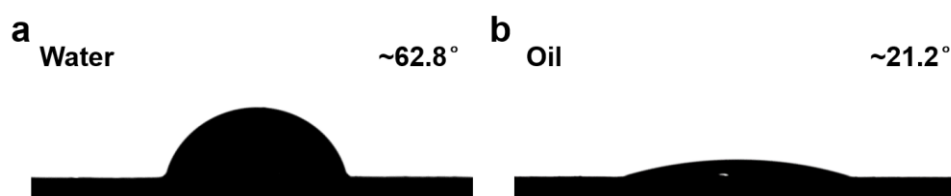


Figure S5. CA images of water (a) and oil (b) on unstructured silicone hydrogels with the SiM content of 40%. The CAs of water and oil on flat silicone hydrogel are $\sim 62.8^\circ$ and $\sim 21.2^\circ$, respectively.

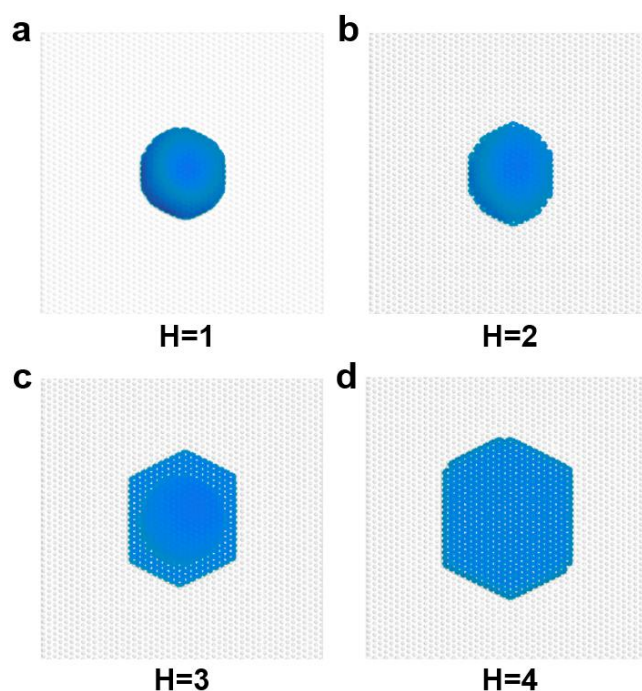


Figure S6. The results of Lattice Boltzmann simulations. (a,b) On nanofibers array shorter than the threshold length ($H=1$ and 2), liquids can not be completely spread out; (c,d) on nanofiber array longer the threshold length ($H=3$ and 4), liquids can completely wet the surface. And the longer nanofiber will result in larger spreading area.

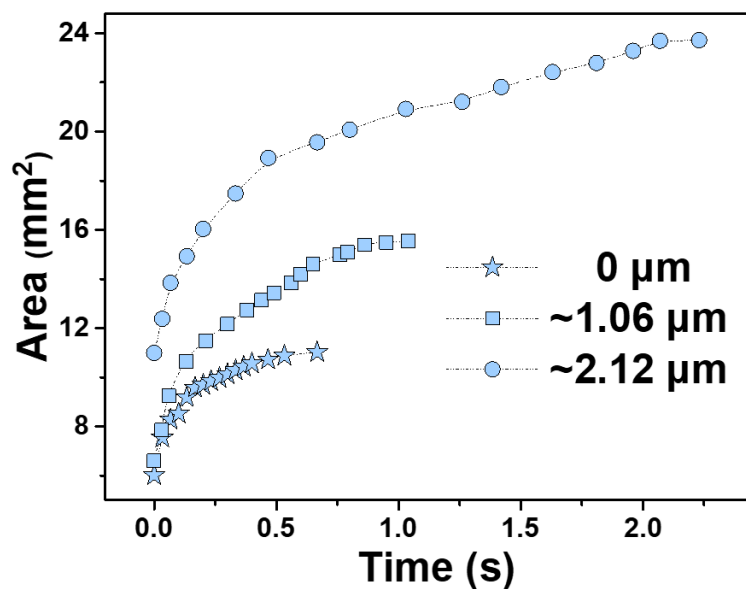


Figure S7. Dynamic spreading on the BSHs. On unstructured silicone hydrogels (0 μm), spreading is soon stopped (within ~ 0.5 s) and a 2 μL water droplet can spread out for ~ 11.02 mm^2 . While on nanofiber array (~ 2.12 μm), a same volume droplet is able to spread out for ~ 23.72 mm^2 until the CA approaches $\sim 0^\circ$.

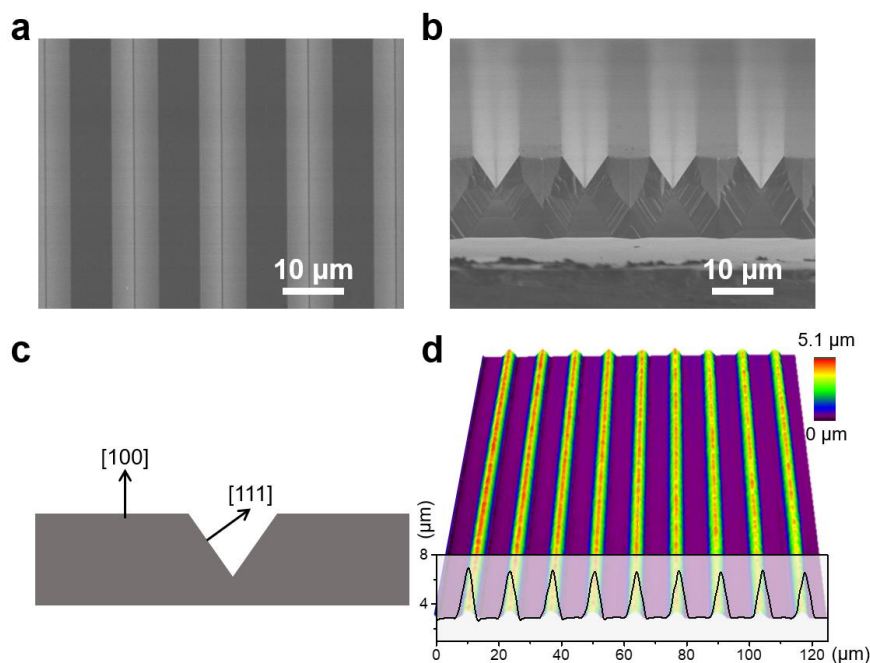


Figure S8. Potassium hydroxide etched silicon wafers with triangular column pits and the imprinted poly(bisphenol A polycarbonate) plates. (a,b) Top-view and oblique-view SEM images of the potassium hydroxide etched triangular column pits in (100) silicon wafers, respectively. The top width and depth of the triangle pits is 7 μm and 5 μm, respectively. (c) The (111) crystal faces on (100) silicon wafer were exposed to form the triangle shape. (d) 3D image of the poly(bisphenol A polycarbonate) plates demolded from the silicon wafer. The inset is the plate section height as a function of distance.

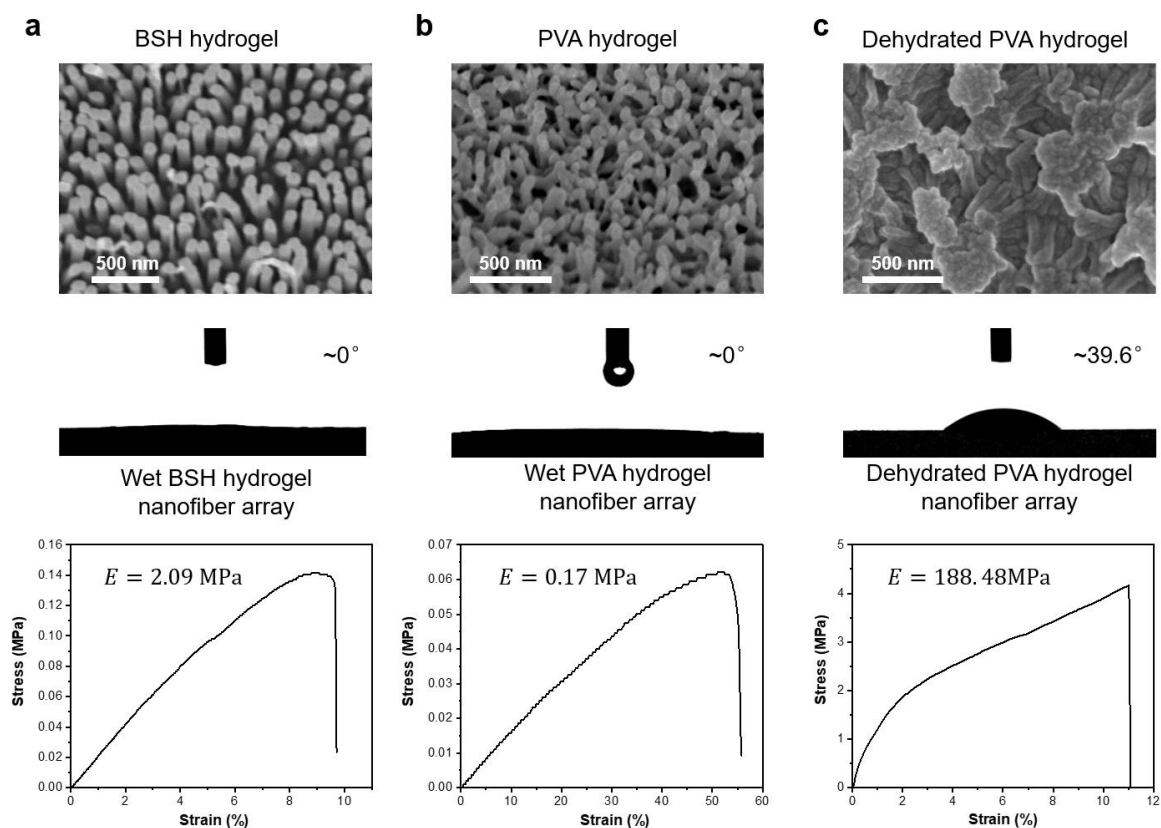


Figure S9. Morphology, wetting state, mechanical properties of BSH, PVA hydrogel and dehydrated PVA hydrogel. (a) SEM images of BSH nanofiber array after freeze-drying, CA image and stress-strain curve of wet BSH hydrogel. (b) SEM images of BSH nanofiber array after freeze-drying, CA image and stress-strain curve of wet PVA hydrogel. (c) SEM image of dehydrated PVA hydrogel nanofiber array after evaporation-drying, CA image and stress-strain curve of the dehydrated PVA hydrogel.

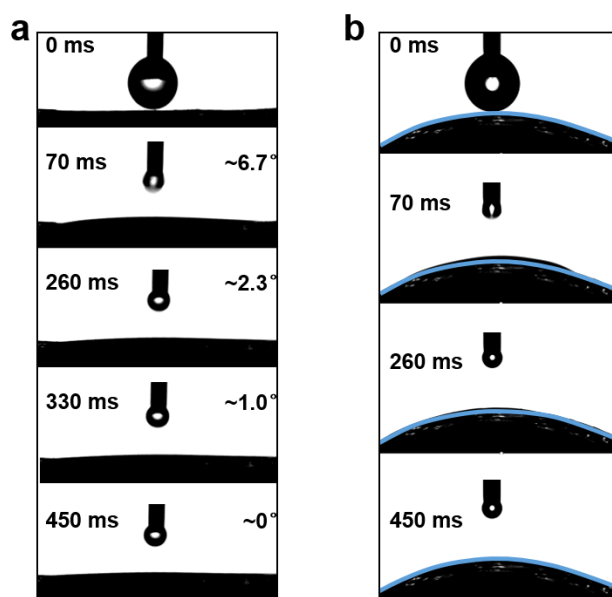


Figure S10. Dynamic superspreading processes of a 2 μL water droplet on PVA hydrogels with microchannel & nanofiber array when the base is flattened (a) and curved with a curvature of 0.15 (b).

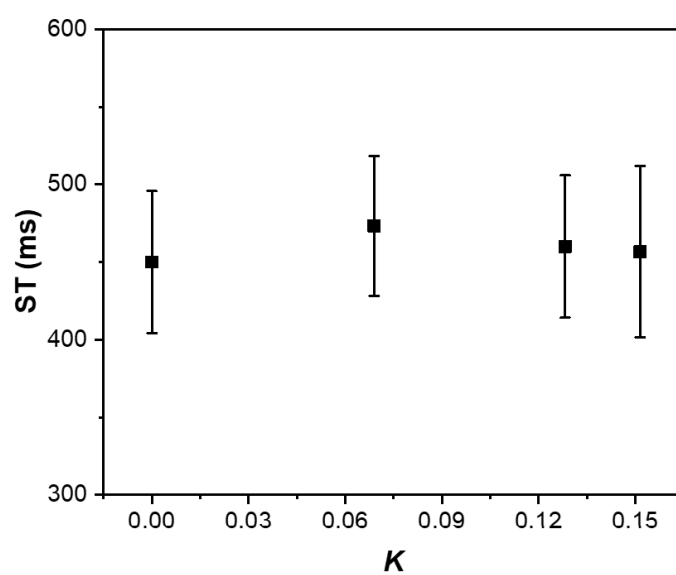


Figure S11. Variation in ST on PVA hydrogel with microchannel & nanofiber array as a function of the curvature (K) of the surface.

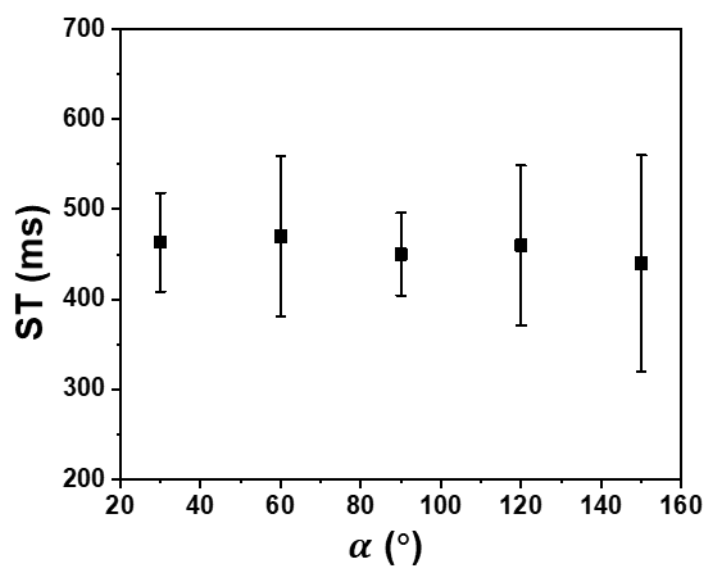


Figure S12. ST as a function of microchannel angle (α). Effect of α on ST is ignorable. Error bars represent the standard deviations ($n = 3$).

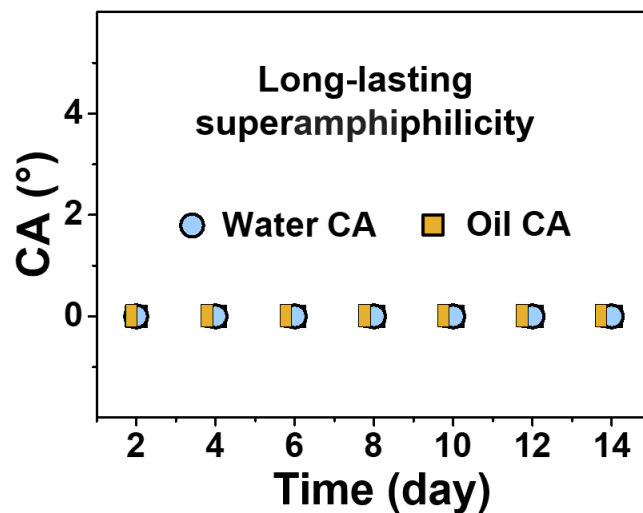


Figure S13. Long-lasting superamphiphilicity of BSH. The water and oil CAs can be kept at about 0° for at least two weeks when the samples are stored in PBS, showing the long-lasting superamphiphilicity of BSH. Error bars represent the standard deviations ($n = 5$).

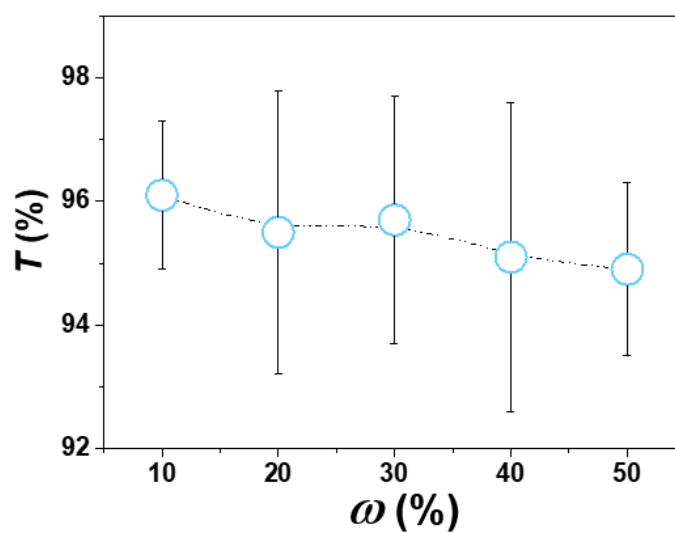


Figure S14. Transparency of BSH as a function of mass fraction of SiM (ω). ω has a little effect on the light transmittance of the hydrated BSH. Error bars represent the standard deviations ($n = 5$).

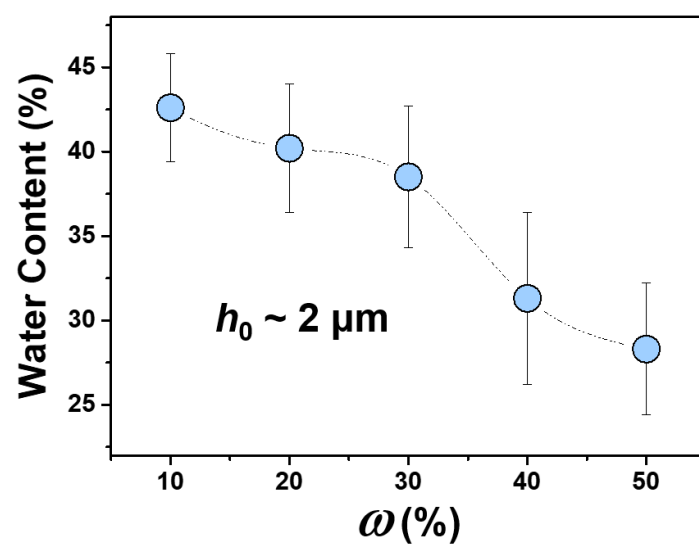


Figure S15. Water content of BSH with different compositions. Increase in the content of SiM will decrease the water content of BSH. Error bars represent the standard deviations ($n = 5$).

Table S1. Monomers ratio for the fabrication of BSHs.

Component	ω (%)				
SiM	10	20	30	40	50
NVP	80	70	60	50	40
HEMA	10	10	10	10	10
PEGDMA	8	8	8	8	8
D-1173	0.4	0.4	0.4	0.4	0.4
1-Hexanol	20	20	20	20	20

Legends for movies S1 to S11:

Movie S1. Water rapid superspreading on the rabbit cornea.

Movie S2. Lateral-view water dynamic spreading on BSH with $\sim 0.5\ \mu\text{m}$ -length nanofiber array.

Movie S3. Lateral-view water dynamic spreading on BSH with $\sim 2.12\ \mu\text{m}$ -length longer nanofiber array.

Movie S4. Lateral-view water dynamic spreading process on flat PVA hydrogel.

Movie S5. *In situ* water dynamic spreading process under microscopy on flat PVA hydrogel.

Movie S6. Lateral-view water dynamic spreading process on PVA hydrogel with microchannels.

Movie S7. *In situ* water dynamic spreading process under microscopy on PVA hydrogel with microchannels.

Movie S8. Lateral-view water dynamic superspreading process on PVA hydrogel with nanofiber array.

Movie S9. *In situ* water dynamic superspreading process under microscopy on PVA with nanofiber array.

Movie S10. Lateral-view water rapid superspreading process on PVA with microchannel & nanofiber array morphology.

Movie S11. *In situ* water rapid superspreading process under microscopy on PVA with microchannel & nanofiber array morphology.

Movie S12. Lateral-view water rapid superspreading process on PVA with microchannel & nanofiber array morphology when the surface is curved with a curvature of 0.15.

.

References

- [1] Doi, M., *Eur. Phys. J. Special Topics* **2016**, 225, 1411-1421.
- [2] Sangani, A. S., Acrivos, A., *Int. J. Multiphase Flow* **1982**, 8, 193-206.
- [3] Ransohoff, T. C., Radke, C. J., *J. Colloid Interface Sci.* **1988**, 121, 392-401.